Published on 17 October 2022. Downloaded by Korea Advanced Institute of Science & Technology / KAIST on 11/27/2022 3:29:05 PM.

Journal of Materials Chemistry A

ROYAL SOCIETY OF CHEMISTRY

PAPER

View Article Online
View Journal | View Issue

Check for updates

Cite this: J. Mater. Chem. A, 2022, 10, 23282

# Galvanic replacement reaction in perovskite oxide for superior chemiresistors†

Jong Won Baek,‡[a] Yoon Hwa Kim,‡[ab] Jaewan Ahn,[a] Dong-Ha Kim,[ac] Hamin Shin,[a] Jaehyun Ko,[a] Seyeon Park,[a] Chungseong Park,[a] Euichul Shin,[a] Ji-Soo Jang*[d] and Il-Doo Kim *[a]

Received 5th July 2022
Accepted 14th October 2022

DOI: 10.1039/d2ta05338a

rsc.li/materials-a

It is well known that certain gas molecules can serve as specific markers for characterizing the physiological and environmental nature of a subject, such as acetylene gas which can be used for determining a person's smoking status as well as for monitoring air pollution levels. For their reliable detection, gas sensors should be designed with high sensing capabilities in terms of selectivity, sensitivity and low detection limit. In this work, we present a rational design approach for the synthesis of p-type $LaFeO_3$/n-type $SnO_2$ composite nanotubes (NTs) *via* galvanic replacement reaction (GRR) on electrospun perovskite $LaFeO_3$ NTs for p–n type-converted sensing. The GRR process provides $LaFeO_3$/$SnO_2$ NTs with high surface area (146.6 $m^2$ $g^{-1}$) by generating $SnO_2$ nanograins (<10 nm), as controlled by varying the reaction time. The abundant heterogeneous p–n junctions formed in $LaFeO_3$/$SnO_2$ NTs contribute to the dramatic improvements in their sensing characteristics. In fact, the $LaFeO_3$/$SnO_2$ NTs exhibited 31.2-fold increased response toward acetylene (5 ppm) with a far improved response speed (16 s) compared to that of pristine $LaFeO_3$ NTs (64 s). Our results demonstrate that the GRR process can be used to engineer the morphology and composition of p-type perovskites to achieve exceptional chemical sensing performances.

## Introduction

In general, the presence of specific gas molecules in the environment, which are generated by various physical, chemical, or biological processes, can be used to report various natural and/or artificial phenomena.[1,2] For rapid and accurate detection of target gas molecules, it is widely accepted that chemiresistive-type gas sensors based on semiconducting metal oxides (SMOs) are especially effective.[3] In a brief description, as gas molecules interact with the surface of the SMO-based sensing material, the surface electronic structure is modulated, resulting in detectable changes in the resistance of the SMO.[4] This allows for high levels of sensitivity and low limits of detection, particularly for sensors based on n-type SMOs (*e.g.*, $SnO_2$, $WO_3$, ZnO).[5,6] However, n-type SMOs generally lack the selectivity toward specific target gas molecules and are overly sensitive to various environmental factors such as humidity and temperature. In this regard, p-type $ABO_3$ perovskites offer two key advantages over conventional n-type SMOs for the development of selective and robust sensors. For one, typical $ABO_3$ perovskites consist of rare-earth metal atoms occupying the A sites and transition metal atoms occupying the B site of the cubic lattice; by tuning the composition of the A and B sites by cation substitution, their physicochemical materials properties can be tuned to modulate their selective sensing behaviors.[7–9] Moreover, as a p-type SMO, $ABO_3$ perovskites are more resilient against fluctuations in the environment in comparison to typical n-type SMOs.[10–12] Despite their advantages, perovskite-based chemiresistive sensors have long been hindered by their inherently slow and/or weak response, largely due to the relatively lower mobility of holes in p-type semiconductors compared to the case of electrons in n-type semiconductors.[12] As such, to enhance the sensing performance of perovskite-based materials, various strategies including doping at A-sites of the perovskite lattice,[13,14] loading of noble metal nanocatalysts,[15] and nanoengineering to increase the surface area and porosity have been explored in the past.[16–18] Even now, there is still outstanding demand for a more efficient and effective processing method for improving perovskite-based sensors for practical applications.

From a recent report, the galvanic replacement reaction (GRR) has been demonstrated as a simple pathway to achieve

[a]Department of Materials Science and Engineering, Korea Advanced Institute of Science and Technology (KAIST), 291 Daehak-ro, Yuseong-gu, Daejeon 34141, Republic of Korea. E-mail: idkim@kaist.ac.kr

[b]Forensic Toxicology & Chemistry, Seoul Institute, National Forensic Service, 139 Jiyang-ro, Yangcheon-gu, Seoul 08036, Republic of Korea

[c]Department of Chemistry, Massachusetts Institute of Technology, 77 Massachusetts Avenue, Cambridge, 02139, Massachusetts, USA

[d]Electronic Materials Research Center, Korea Institute of Science and Technology, Seoul 02792, Republic of Korea. E-mail: wkdwltn92@kist.re.kr

† Electronic supplementary information (ESI) available. See DOI: https://doi.org/10.1039/d2ta05338a

‡ These authors contributed equally to this work.



This journal is © The Royal Society of Chemistry 2022

Published on 17 October 2022. Downloaded by Korea Advanced Institute of Science & Technology / KAIST on 11/27/2022 3:29:05 PM.

fine control over the elemental composition and porosity of metal oxide nanostructures.[19] In the context of metal oxides, GRR consists of a pair of redox reactions driven by the difference in electrochemical potentials of two dissimilar metal species, during which the species with the higher reduction potential is dissolved from the parent structure *via* reduction while the other is deposited onto the surface of the parent structure *via* the formation of oxides. As a result, the parent metal oxide transforms into a porous nanostructure *via* localized dissolution of the oxide matrix while the secondary phase is grown on the surface of the parent metal oxide. By applying GRR through a simple wet chemistry experiment, we hypothesized that the electronic properties and surface reactivity of the perovskite-based sensing material could simultaneously be enhanced. Our hypothesis is supported by several case studies including the work by Jeong *et al.*, who applied the GRR to convert p-type $Co_3O_4$ hollow spheres into $Co_3O_4/SnO_2$ spheres, whereby controlling the Sn concentration could determine the gas selectivity.[20] Likewise, Jang *et al.* reported the synthesis of 3D $Co_3O_4/SnO_2$ hollow structures *via* GRR of zeolitic imidazolate framework-67 (ZIF-67)-derived $Co_3O_4$ polyhedron as well as the fabrication of 2D $Co_3O_4/SnO_2$ derived from exfoliated $Co_3O_4$ nanosheets.[21,22] Altogether, we propose that GRR could be used to fine-tune the physical and chemical nature of perovskites and enhance their gas sensing properties.

In this work, we demonstrate the efficacy of GRR treatment for the development of porous nanostructures and the creation of abundant p–n heterointerfaces on $LaFeO_3$ perovskite nanotubes (NTs) for use as effective sensor materials. Herein, $LaFeO_3$ NTs prepared by electrospinning and subsequent calcination were allowed to react with Sn(II) ions in a simple aqueous reaction. Due to the asymmetry in the amounts of materials dissolved from the oxide nanofibers *versus* deposited on the oxide surface during GRR, numerous mesopores were formed in the resulting $LaFeO_3/SnO_2$ composite structure. To gain a mechanistic understanding of the synthesis process, we systematically analyzed the time-dependent changes in the composition as well as structural evolution behaviors upon GRR. We further demonstrate that porous $LaFeO_3/SnO_2$ NTs can be fabricated into a gas sensor that exhibits high sensitivity, low limit of detection, and high selectivity to the target gas (acetylene), as we had hypothesized. Altogether, we showed that the GRR-based method is a facile and effective approach to the fabrication of perovskite-based heterogeneous oxide nanostructures with high porosity and tailored compositions, combining the high selectivity and robustness of p-type perovskites with the high response of n-type oxides. Selectivity and robustness of p-type perovskites with the high response of n-type oxides.

## Results and discussion

Fig. 1a presents a schematic illustration describing the synthesis of hollow $LaFeO_3/SnO_2$ nanotubes by means of the GRR process (hereafter, $LaFeO_3/SnO_2$ NTs). We first prepared polyvinylpyrrolidone (PVP)-based composite nanofibers (NFs) containing La and Fe precursors using a single-spinneret electrospinning method. Then, the electrospun NFs were calcined in ambient air at 450 °C, then again for a second time at 700 °C to obtain polycrystalline perovskite $LaFeO_3$ NTs, following a previous report.[23] Subsequently, we initiated the galvanic replacement reaction (GRR) process by mixing the as-prepared $LaFeO_3$ NTs into a Sn precursor solution, which resulted in the dissolution of portions of $LaFeO_3$ and the simultaneous deposition of n-type $SnO_2$ nanograins on the surface of NTs. Based on the electrochemical reduction potentials of each pair of redox species in the system, including $Fe^{3+}/Fe^{2+}$ (0.77 V), $Sn^{4+}/Sn^{2+}$ (0.15 V), $SnO_2/Sn^{2+}$ (−0.09 V), and $La^{3+}/La$ (−2.38 V) pairs, the GRR between $Fe^{3+}$ and $Sn^{2+}$ as well as between $Sn^{2+}$ and $La^{3+}$ could be described by the following set of reactions:

$$2Fe^{3+} + Sn^{2+} \rightarrow 2Fe^{2+} + Sn^{4+} \ (E^\circ = 0.62\ V) \quad (1)$$

$$3Sn^{2+} + 2La^{3+} \rightarrow 3Sn^{4+} + 2La \ (E^\circ = -2.53\ V) \quad (2)$$

Following eqn (1), we could deduce that a spontaneous precipitation of $SnO_2$ nanograins on the surfaces of $LaFeO_3$ NTs would occur concomitantly with dissolution of Fe from $LaFeO_3$ NTs. Specifically, one $Sn^{2+}$ ion from the $SnCl_2$ salt is oxidized to $Sn^{4+}$ for the formation of $SnO_2$, which generates six electrons in the process. In turn, these electrons are used to reduce two $Fe^{3+}$ ions in the $LaFeO_3$ matrix to $Fe^{2+}$ species as elucidated in eqn (1). On the other hand, the GRR between $Sn^{2+}$ and $La^{3+}$ ions is not likely to occur because the $La^{3+}/La$ species possess a much lower standard potential compared to that of the Sn species (*i.e.*, cell potential for the reaction in eqn (2) is negative). However, the chloride ions present in the solution, especially in the form of additional HCl, can aid in the etching of La for their dissolution from the surface of $LaFeO_3$ NTs. Therefore, the perovskite $LaFeO_3$ phase could be replaced in part by the $SnO_2$ to produce multi-phase composite nanotubes.

To study the mechanism of GRR-induced transformation from the viewpoint of morphology and composition of the NFs, we utilized a precursor solution based on $Sn^{2+}$ ions (2 M) and varied the reaction times from 0 to 10, 30, or 120 min, hereafter denoted as 0, 10, 30 and 120_$LaFeO_3/SnO_2$ NTs, respectively. The scanning electron microscope (SEM) image in Fig. 1b clearly shows the hollow structure of pristine $LaFeO_3$ NTs (0_$LaFeO_3/SnO_2$ NTs). A digital camera image of 0_$LaFeO_3/SnO_2$ NTs dispersed in xylene shows a deep brown color (inset of Fig. 1b), which corresponds to that of apparent colors of $LaFeO_3$ powder.[24] To investigate the microstructures of the $LaFeO_3/SnO_2$ NTs, transmission electron microscopy (TEM) analysis was carried out. The TEM image of 0_$LaFeO_3/SnO_2$ NTs (Fig. 1c and S1†) reveals large aspect ratio 1D nanostructures, with lengths over 1 μm and an average width of 100–200 nm. Furthermore, the high-resolution TEM (HRTEM) image shown in Fig. 1d indicates a crystallized structure with interplanar distances of 0.394 nm, which corresponds to that of the (101) plane in $LaFeO_3$.[25] The overall hollow nanostructure of $LaFeO_3$ NTs promotes the large-scale diffusion of $Sn^{2+}$ ions to the interior of $LaFeO_3$ NTs to facilitate the GRR even on the inner

Published on 17 October 2022. Downloaded by Korea Advanced Institute of Science & Technology / KAIST on 11/27/2022 3:29:05 PM.

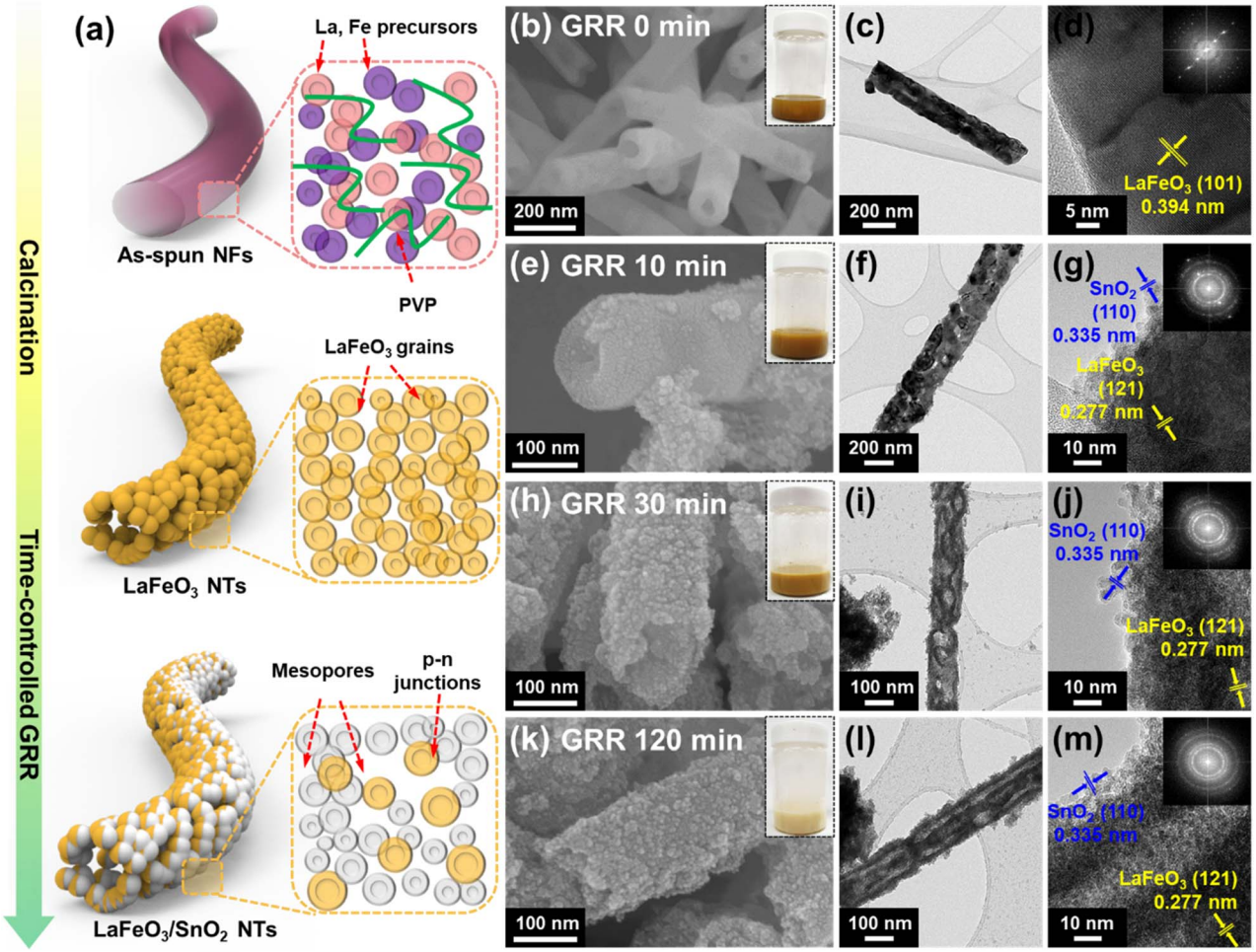


Fig. 1 (a) Schematic representation of synthetic process for $LaFeO_3/SnO_2$ NTs. (b) SEM images with digital camera images of suspension (respective insets), (c) TEM images and (d) HRTEM lattice spacing images (Inset fig. shows the corresponding fast Fourier transform (FFT) patterns) of 0_$LaFeO_3/SnO_2$ NTs, (e), (f), (g) of 10_$LaFeO_3/SnO_2$ NTs, (h), (i), (j) of 30_$LaFeO_3/SnO_2$ NTs and (k), (l), (m) of 120_$LaFeO_3/SnO_2$ NTs, respectively.

surfaces of NTs for a more uniform reaction. Fig. 1e, h and k show the SEM images of the $LaFeO_3$ NTs upon different periods of GRR treatment. When the $Sn^{2+}$ ions in the solution continuously react with the suspended $LaFeO_3$ NTs for 10 min (10_$LaFeO_3/SnO_2$ NTs), $SnO_2$ grains start to form on the surface of $LaFeO_3$ NTs (Fig. 1e). The color of the 10_$LaFeO_3/SnO_2$ NTs solution remains brown (inset in Fig. 1e), similarly to that of 0_$LaFeO_3/SnO_2$ NTs. This indicates that 10 min of GRR was insufficient to sufficiently change the morphology and composition of NTs for altering their optical properties. Nevertheless, the presence of $SnO_2$ particles on the surface of 10_$LaFeO_3/SnO_2$ NTs was clearly observed, indicating the GRR was rapidly initiated upon introduction of $Sn^{2+}$ ions (Fig. 1f and g). When GRR continued for longer durations, *i.e.*, 30 and 120 min, an obvious morphological change in $LaFeO_3$ NTs was observed. After the GRR of $LaFeO_3$ NTs for 30 min (30_$LaFeO_3/SnO_2$ NTs), the highly rough surface could be observed (Fig. 1h and i). In the case of 120_$LaFeO_3/SnO_2$ NTs, a large number of $SnO_2$ particles were observed on the surface (Fig. 1k and l). Interestingly, the color of the $LaFeO_3/SnO_2$ NTs suspension shows a noticeable change from brown-red to white as the GRR time is increased from 0 to 120 min (Fig. S2†), indicating a progressive increase in the amount of $SnO_2$ formed by GRR. Note that HRTEM images shown in Fig. 1g and j and m clearly display an existence of precipitated nanoscale (1–10 nm) $SnO_2$ grains, at which the interplanar distances were measured to be 0.335 nm, corresponding to (110) crystal planes of $SnO_2$.[26] In addition to the formation of $SnO_2$ nanograins on $LaFeO_3$ NTs, the porosity of $LaFeO_3/SnO_2$ NTs was also developed during the GRR process as shown in Fig. 1c, f, i and l.[19] The orientations of numerous $SnO_2$ nanograins are fairly random that these planes corroborated the perspective fast Fourier transform (FFT) patterns (see insets in Fig. 1k–m).

To further investigate the compositional changes in $LaFeO_3/SnO_2$ NTs (0, 10, 30 and 120_$LaFeO_3/SnO_2$ NTs) during the GRR process, energy-dispersive X-ray spectroscopy (EDS) analysis was carried out using a scanning transmission electron microscope (STEM). STEM images of 0, 10, 30 and 120_$LaFeO_3/SnO_2$ NTs clearly show the hollow structures as well as the development of porosity in $LaFeO_3/SnO_2$ NTs as the GRR progresses

 This journal is © The Royal Society of Chemistry 2022

Published on 17 October 2022. Downloaded by Korea Advanced Institute of Science & Technology / KAIST on 11/27/2022 3:29:05 PM.

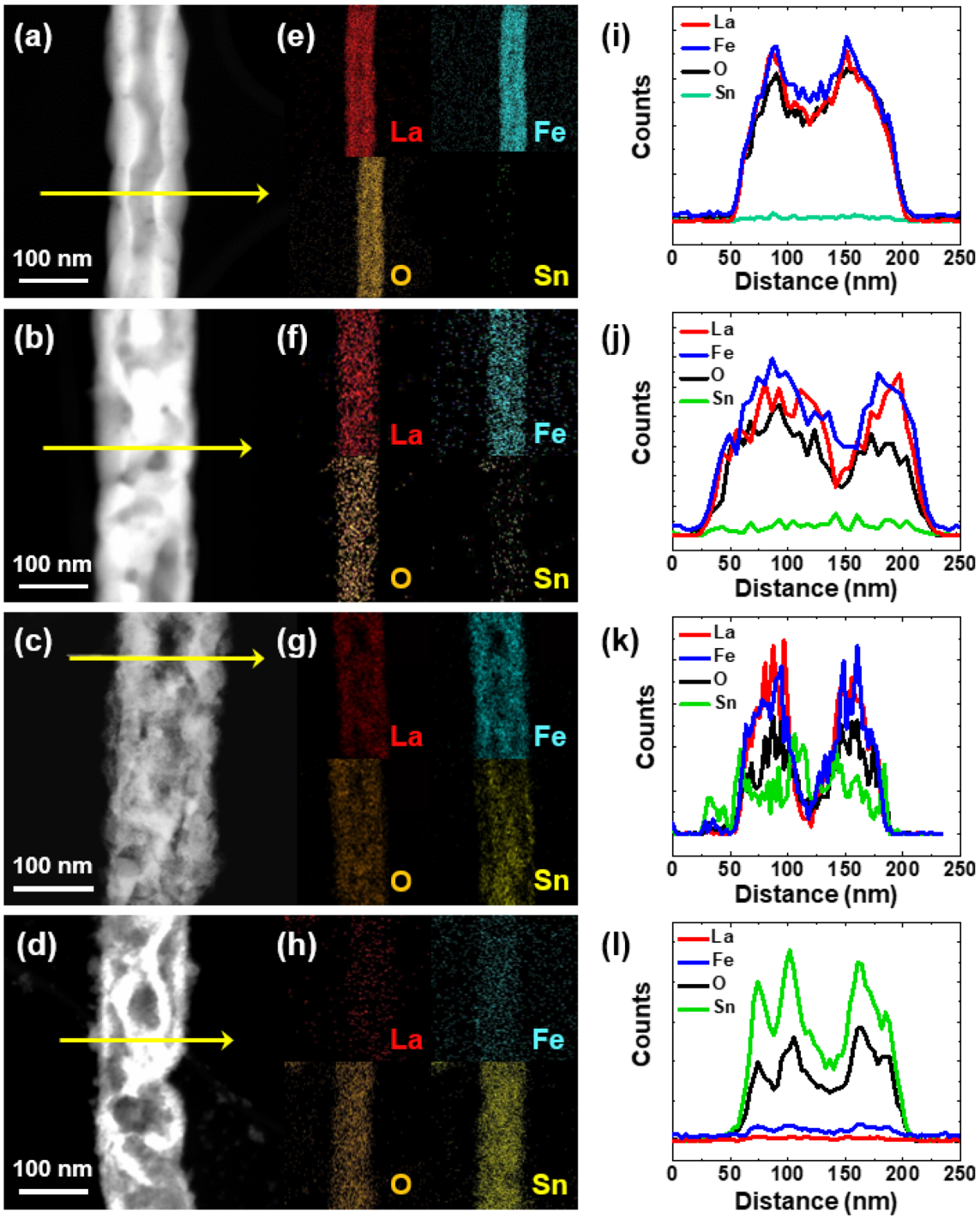


Fig. 2 Scanning TEM (STEM) images of (a) 0, (b) 10, (c) 30, (d) 120_$LaFeO_3/SnO_2$ NTs. Elemental mapping of La, Fe, O and Sn of (e) 0, (f) 10, (g) 30, (h) 120_$LaFeO_3/SnO_2$ NTs. Data plots of the EDS line-scan of (i) 0, (j) 10, (k) 30, (l) 120_$LaFeO_3/SnO_2$ NTs.

(Fig. 2a–d). In the case of 0_$LaFeO_3/SnO_2$ NTs (Fig. 2e), the mapping result reveals uniform distributions of La, Fe and O elements, corresponding to pristine $LaFeO_3$ NTs. After initiating the GRR, as shown in Fig. 2f–h, the visible peak intensity of Sn is gradually increased as a function of the reaction time, even surpassing that of La and Fe after 120 min as a result of the continuous dissolution of $LaFeO_3$ NTs and the simultaneous formation of $SnO_2$ nanograins on the surface of $LaFeO_3$ NTs. The relative atomic ratio of Sn to the sum of La and Fe was increased from 0 to 5.20 (Fig. S3†), indicating that Sn can become the dominant component in $LaFeO_3/SnO_2$ NTs after 120 min of GRR process. To further explore the morphological evolution of $SnO_2$ on the surface of $LaFeO_3$ NTs during the GRR, the EDS line-scan profile analysis was also conducted (Fig. 2i–l).

Published on 17 October 2022. Downloaded by Korea Advanced Institute of Science & Technology / KAIST on 11/27/2022 3:29:05 PM.

As shown in data plots of Fig. 2i, the 0_$LaFeO_3/SnO_2$ NTs only show La, Fe and O components. Upon addition of the $Sn^{2+}$ ion precursor solution, the Sn signals start to appear within 10 minutes, as seen from Fig. 2j. Furthermore, 30_$LaFeO_3/SnO_2$ NTs show a substantial increase in the Sn signal with respect to the other transition metals, suggesting that major portions of $LaFeO_3$ were transitioned to $SnO_2$ by GRR (Fig. 2k). By 120 minutes, only a minor amount of $LaFeO_3$ phase could be found, while the majority of the signals were contributed by Sn (Fig. 2l).

In order to investigate the evolution of the crystal structures during the transformation of $LaFeO_3$ NTs into $LaFeO_3/SnO_2$ NTs at different stages of the GRR process, we conducted powder X-ray diffraction (PXRD) analysis of $LaFeO_3/SnO_2$ NTs as a function of GRR treatment time. As a reference, the distinctive peaks of 0_$LaFeO_3/SnO_2$ NTs could be indexed to the orthorhombic $LaFeO_3$ phase (JCPDS# 37-1493), which are shown as black lines in Fig. 3a. Here, we observed that the average grain size of $LaFeO_3$ is 39.7 nm, according to the Scherrer formula (Table S1†). After 10 min of GRR, there were no noticeable changes in the peak positions and intensities, indicating that the amount of $SnO_2$ formed at this stage is very limited (10_$LaFeO_3/SnO_2$ NTs; see orange line). After 30 min, a characteristic peak associated with tetragonal $SnO_2$ (JCPDS# 41-1445) started to appear in the low-angle region, indicating the presence of $SnO_2$ throughout the nanostructure. The Scherrer formula indicated that the $SnO_2$ phase existed in grains having sizes around 3.0 nm (Table S1†). By this fact, smaller $SnO_2$ nanograins can lead to higher gas response in gas sensing applications. Once the NTs were treated for 120 min, the tetragonal $SnO_2$ peaks became dominant, while the peaks of $LaFeO_3$ phase were no longer recognizable. Moreover, the peak widths were significantly broadened in the case of 120_$LaFeO_3/SnO_2$ NTs, which indicates that the nanostructure has overall been refined to smaller grain sizes. Also, we further confirmed that the ratio of

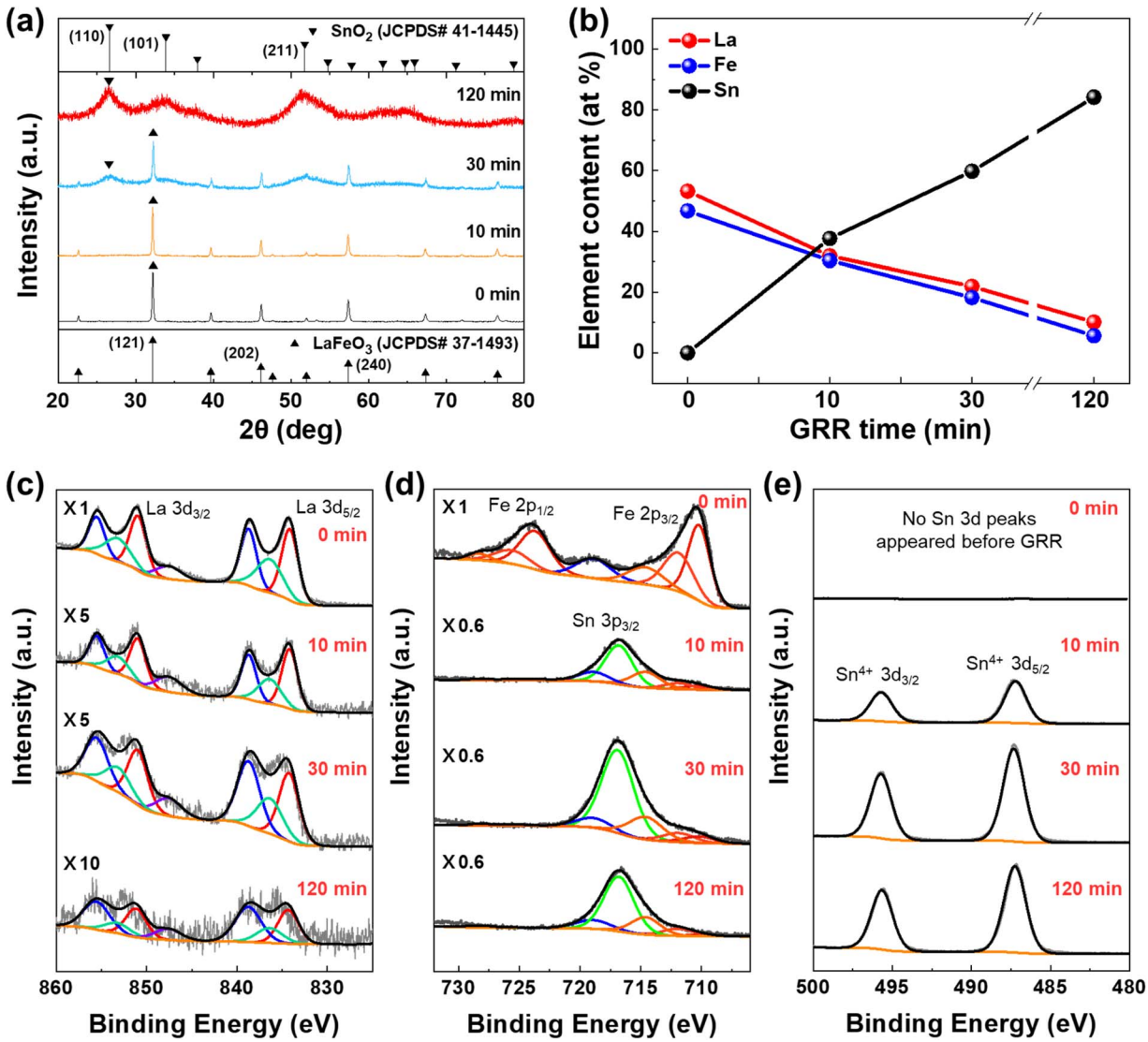


Fig. 3 (a) XRD patterns from $2\theta = 20–80°$ for 0, 10, 30 and 120_$LaFeO_3/SnO_2$ NTs. (b) ICP-OES data of La, Fe and Sn for 0, 10, 30 and 120_$LaFeO_3/SnO_2$ NTs. *Ex situ* XPS spectra of (c) La 3d, (d) Fe 2p, Sn 3p (e) Sn 3d in 0, 10, 30 and 120_$LaFeO_3/SnO_2$ NTs.

 This journal is © The Royal Society of Chemistry 2022

Published on 17 October 2022. Downloaded by Korea Advanced Institute of Science & Technology / KAIST on 11/27/2022 3:29:05 PM.

XRD peak intensities of $SnO_2$ (110) to $LaFeO_3$ (121) is gradually increased from 0.01 (0 min) to 0.05 (10 min), 0.42 (30 min), and 1.4 (120 min), as shown in Fig. S4.† These results are attributed to the unique effect of GRR which took place at relatively low temperature (<90 °C), thus for, it could prevent severe grain growth of $SnO_2$ nanograins on the support of $LaFeO_3$ NTs.

Furthermore, the inductively coupled plasma optical emission spectroscopy (ICP-OES) analyses were conducted to quantitatively measure the content of each element (at%, atomic percent) as a function of the GRR time. If our hypothesis is valid, the amount of La and Fe in the $LaFeO_3$ NTs should gradually decrease, reflecting their dissolution, and the amount of Sn should increase, reflecting their deposition. Fig. 3b shows that the amount of La and Fe in the $LaFeO_3$ NTs decreased from 53.24 to 10.14 at% and from 46.75 to 5.67 at%, respectively, as the reaction time of GRR was increased from 0 min to 120 min. In comparison, the amount of Sn in the $LaFeO_3$ NTs increased from 0 to 84.19 at% as the reaction time was increased from 0 min to 120 min. This result indicates that the composition of the final product could be manipulated by simply controlling the GRR time.

In addition to ICP-OES results, X-ray photoelectron spectroscopy (XPS) was examined to elucidate the detailed chemical states of each element for $LaFeO_3/SnO_2$ NTs at different stages of the GRR process. The La 3d doublet peaks were located at 834.0 and 850.8 eV (Fig. 3c), which are respectively attributed to the $3d_{5/2}$ and $3d_{3/2}$ energy levels of La in the oxidized state.[27] The spin–orbit splitting gap of 16.8 eV between $3d_{5/2}$ and $3d_{3/2}$ peaks specifically indicates the $La^{3+}$ valence state. The remaining four peaks can be ascribed to the satellite peaks of La 3d. Interestingly, the relative prevalence of each species of La as well as their peak positions were mostly preserved as the GRR progressed from 0 to 120 min, although the overall intensity was diminished by 120 min. In the Fe 2p region, Fe cations are in a mixed valence state of $Fe^{2+}$, $Fe^{3+}$ and $Fe^{4+}$, even though an ideally stoichiometric perovskite $LaFeO_3$ should consist solely of $Fe^{3+}$. This is because the La vacancies in $LaFeO_3$ lattice may promote the formation of $Fe^{4+}$ or oxygen vacancies in order to maintain the charge neutrality.[28] Considering just the $Fe^{3+}$ species, the binding energies of Fe $2p_{3/2}$ and Fe $2p_{1/2}$ were observed at 710.2 eV and 723.7 eV with a satellite peak of $Fe^{3+}$ at 718.9 eV (Fig. 3d), all of which appropriately corresponds to the characteristic peaks of $Fe^{3+}$ ions in their oxide form.[27] The overall intensity of Fe 2p XPS was diminished as the reaction progressed from 0 to 120 min (Fig. S5† for magnified *y*-axis scale). In the case of Sn, after 30 min of GRR treatment, we could identify the characteristic doublet peaks of $Sn^{4+}$ at 487.3 eV and 495.8 eV, respectively assigned to Sn $3d_{5/2}$ and Sn $3d_{3/2}$ peaks (Fig. 3e).[29,30] Moreover, a new peak also appeared at 716.9 eV, assigned to the Sn $3p_{3/2}$ peak of $Sn^{4+}$, which was notably overlapped with the Fe 2p signals. These results evidently support the successful formation of the n-type $SnO_2$ phase on the surface of $LaFeO_3$ NTs by GRR.[31,32] Importantly, while the signal intensity of the $Sn^{4+}$ related peaks remain relatively strong throughout the GRR process, the signal intensity of the La 3d and Fe 2p peaks gradually decreased as the GRR treatment continued, indicating the simultaneous dissolution of La and Fe from the NTs lattice.[28] Fig. S6† shows the deconvoluted O 1s spectra for $LaFeO_3$ NTs, wherein 0_$LaFeO_3/SnO_2$ NTs were shown to have three main peaks, one at 529.3 eV which is assigned to the lattice O atoms ($O^{2-}$) in $LaFeO_3$ and other one at 531.2 eV representing the adsorbed oxygen ($O^-$) and physisorbed species ($O_2^-$) at 532.6 eV.[33,34] After the onset of GRR, the peak at 530.3 eV is assigned to the lattice O atoms in $SnO_2$ and 531.2 eV represents adsorbed ionized oxygen on the $SnO_2$ surface. Also, physisorbed species ($O_2^-$) are also formed on the $SnO_2$ surface in air at 532.6 eV.[35] Taken together, it is evident that the GRR process could be utilized to replace the $LaFeO_3$ phase with the $SnO_2$ phase, and that the extent of this compositional modulation can effectively be controlled by tailoring the reaction time.

In the end, we can effectively tune both the morphology and composition of the GRR-driven heterogeneous $LaFeO_3/SnO_2$ NTs to optimize their properties for specific applications. In particular, the two critical extensive parameters tuned by the GRR process that needs to be considered for chemiresistive sensing is: (1) the modulation of electrical properties of the constituent SMOs; and (2) the change in the microstructures of the SMOs. As shown in Fig. 4a, the interface between $SnO_2$ ($d_{110}$ = 0.335 nm) and $LaFeO_3$ ($d_{121}$ = 0.277 nm) was found to be highly coherent according to the HRTEM analysis, the ultraviolet photoelectron spectroscopy (UPS) and ultraviolet-visible (UV-vis) spectroscopy measurements for $LaFeO_3$ and $SnO_2$ samples identified the work functions and band gap of $LaFeO_3$ (work function = 6.24 eV, band gap = 2.25 eV), and $SnO_2$ (work function = 5.22 eV, band gap = 3.62 eV), respectively (Fig. S7 and S8†). A simplified energy band diagram of the $LaFeO_3$ and $SnO_2$ is shown in Fig. S9.† The formation of p–n heterojunctions and corresponding electron depletion regions formed by diffusion of the majority holes in $LaFeO_3$ and the electrons in $SnO_2$ toward opposite directions to each other as illustrated in band structures (Fig. 4b). Moreover, it is well known that the grain size of nanostructured gas sensing materials has a major influence on their response.[36] Note that the gas response (defined as the resistance of the sensing material exposed to the target gas normalized by its resistance in ambient air) can be enhanced as the grain size of nanostructured gas sensing materials is decreased, since it results in an increase of the total active surface area. Thus, the dramatic modulation of electron depletion regions can be achieved.[37] In our case, the 30_$LaFeO_3/SnO_2$ NTs showed a substantially increased Brunauer–Emmett–Teller (BET) surface area (146.6 $m^2\ g^{-1}$) compared to that of 0_$LaFeO_3/SnO_2$ NTs (8.0 $m^2\ g^{-1}$), as presented in Fig. 4c. This microstructural evolution of $LaFeO_3$ NTs can be explained by the increase of gas-accessible surface area resulting from the dissolution of the parent $LaFeO_3$ phase and the simultaneous growth of $SnO_2$ nanograins (<5 nm) occurring at random across various sites in the surface of the NTs upon GRR, as shown in Fig. S10.† Furthermore, the pore volume of 30_$LaFeO_3/SnO_2$ NTs (0.25 $cm^3\ g^{-1}$) were significantly increased compared with that (0.03 $cm^3\ g^{-1}$) of 0_$LaFeO_3/SnO_2$ NTs (Fig. 4d). In particular, abundant meso-sized pores (2–20 nm) on surfaces of $LaFeO_3/SnO_2$ NTs were created significantly after GRR 30 min. This porous structure not only allows the permeation of Sn

Published on 17 October 2022. Downloaded by Korea Advanced Institute of Science & Technology / KAIST on 11/27/2022 3:29:05 PM.

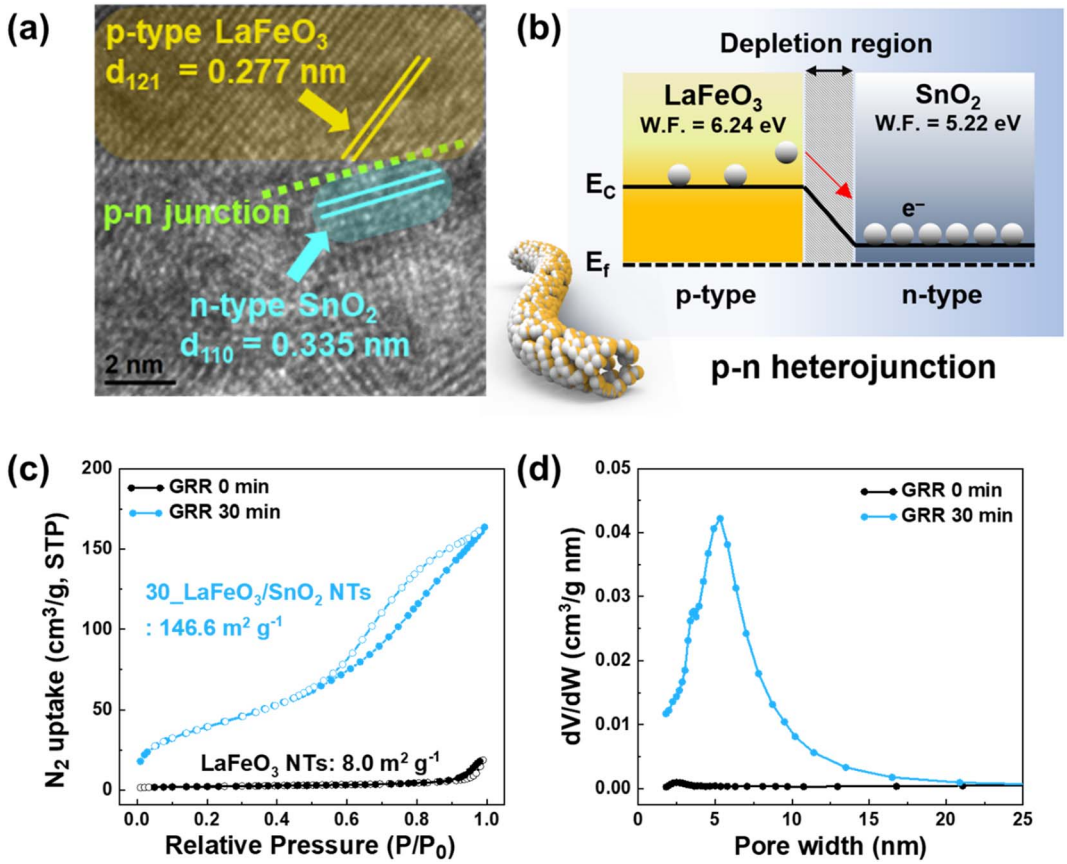


Fig. 4 (a) TEM image of p–n junction between $SnO_2$ and $LaFeO_3$. (b) Schematic illustration of the band structure of $LaFeO_3/SnO_2$ NTs. (c) Brunauer–Emmett–Teller (BET) and (d) Pore size distribution of 0 and 30_$LaFeO_3/SnO_2$ NTs.

solutions onto both inner and exterior sides of $LaFeO_3$ NTs, but also facilitate gas diffusion into the sensing layer.

As a demonstration of the GRR-derived $LaFeO_3/SnO_2$ NTs for gas sensing applications, we prepared gas sensors based on 0, 10, 30 and 120_$LaFeO_3/SnO_2$ NTs and comparatively evaluated their sensing performances. For this study, we selected acetylene as the target species because of its particularly wide applicability as a reporter molecule in many diverse fields. For instance, acetylene could be detected in electrical power transformers as a result of the degradation of transformer oil upon the increased frequency of electric arc generation, indicating that their service life had been reached.[38] Also, acetylene is present in the exhaled breath of smokers in significantly higher concentrations compared to that of non-smokers with values up to 260 ppb from those that smoke.[39,40] Furthermore, concentrated acetylene poses a fire hazard due to its flammability, which necessitates the early detection of possible leaks from pressurized containers.[41] To fabricate the sensors, we first dispersed the as-obtained $LaFeO_3/SnO_2$ NTs in ethanol by sonication to prepare the ink, which was then drop-coated onto an alumina ($Al_2O_3$) sensor substrate and dried (Fig. S11†). All sensing measurements were carried out under 80% relative humidity (R.H.) conditions using a homemade system (Fig. S12†), considering the potential application toward rapid health screening in which acetylene gas can be detected from human exhaled breath.[42]

The graphs in Fig. 5a show the dynamic changes in the resistance of the 0, 10, 30 and 120_$LaFeO_3/SnO_2$ NTs sensors toward 5 ppm of acetylene analyte at 440 °C. It is clear that the formation of the n-type $SnO_2$ phase on $LaFeO_3$ NTs upon GRR induces an electrical type transition to n-type with improved response to acetylene gas, in reference to the p-type pristine

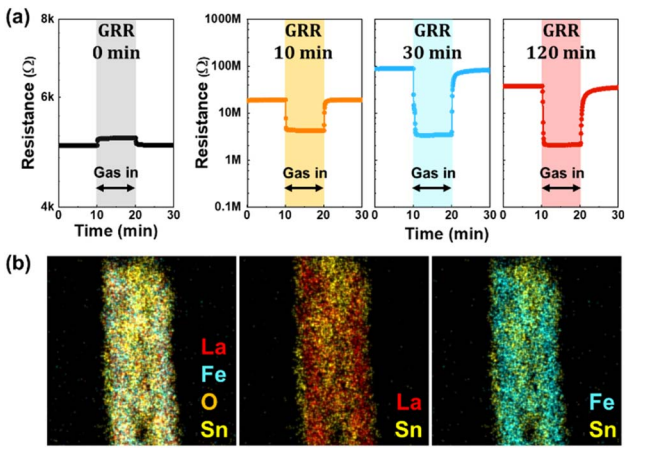


Fig. 5 (a) Dynamic changes in electrical resistance of the 0, 10, 30 and 120_$LaFeO_3/SnO_2$ NTs sensors at 5 ppm of acetylene gas. (b) EDS mapping of the La/Fe/O/Sn, La/Sn and Fe/Sn in 30_$LaFeO_3/SnO_2$.

 This journal is © The Royal Society of Chemistry 2022

Published on 17 October 2022. Downloaded by Korea Advanced Institute of Science & Technology / KAIST on 11/27/2022 3:29:05 PM.

$LaFeO_3$ NTs (see in black line). In addition, the baseline resistances of GRR treated $LaFeO_3/SnO_2$ NTs are three to four orders of magnitude higher than that (5 kΩ) of 0_$LaFeO_3/SnO_2$ NTs, signifying the effect of the $SnO_2$ phase on the electrical properties of the parent $LaFeO_3$ phase. This is supported by the EDS mapping images shown in Fig. 5b, which reveal that Sn is concentrated at the exterior surfaces of the NT nanostructure while the La and Fe are found in the interior of $LaFeO_3$ NTs. This can induce a distinctively higher baseline resistance as a result of thicker electron depletion region by energy band bending and make it more sensitive to gas molecule induced charge transfer.[43,44] Also, the high porosity of 30_$LaFeO_3/SnO_2$ NTs also contributes to the increase in baseline resistance since it decreases the number of electron conduction pathways.

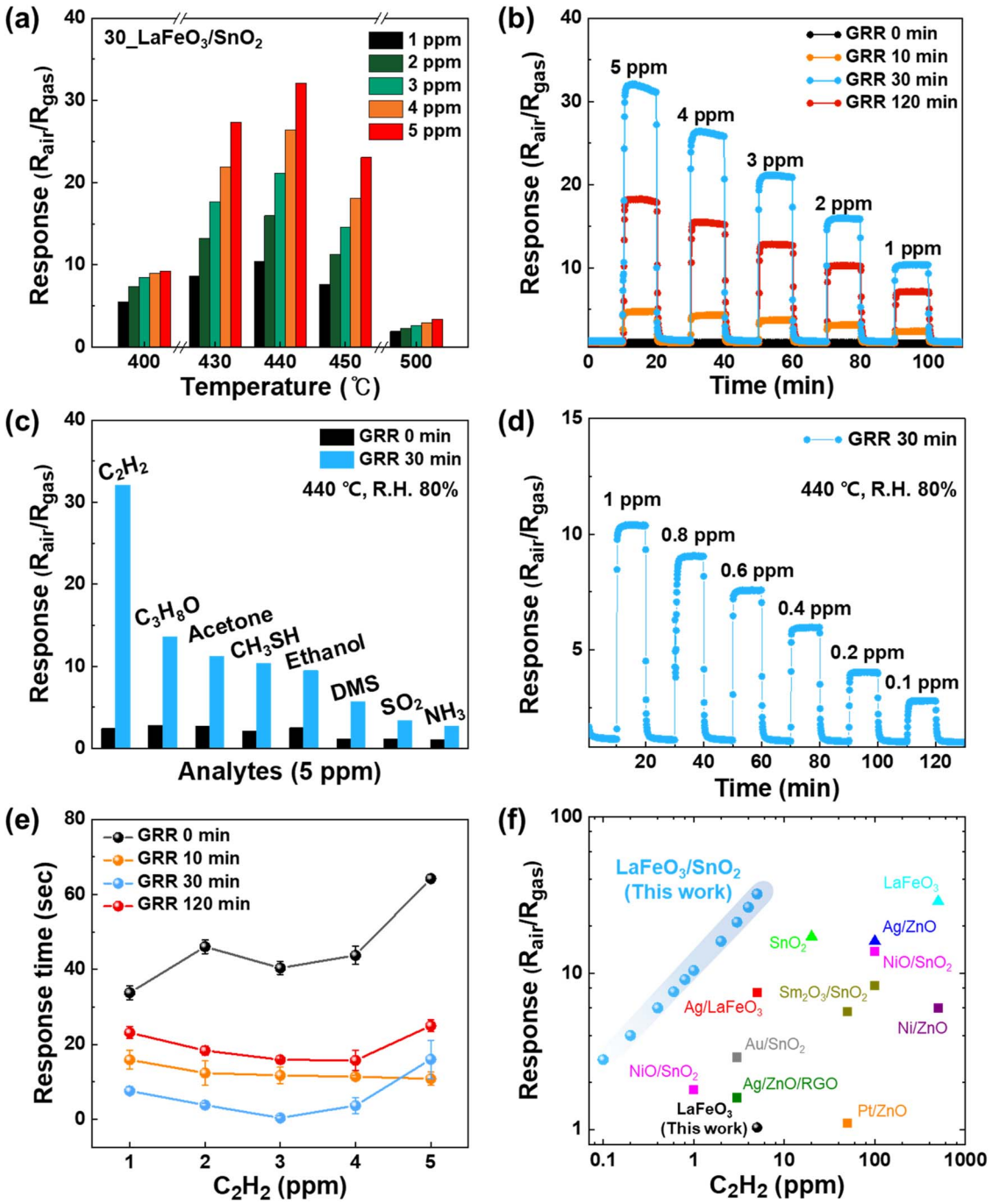


Fig. 6 (a) Sensor response of 30_$LaFeO_3/SnO_2$ NTs for different concentrations of $C_2H_2$ at 400 °C, 430 °C, 440 °C, 450 °C and 500 °C in 80% relative humidity condition. (b) Dynamic $C_2H_2$ gas response in a concentration ranging 1–5 ppm at 440 °C. (c) Selective $C_2H_2$ sensing characteristics of 0 and 30_$LaFeO_3/SnO_2$ NTs with respect to interfering analytes at concentration of 5 ppm at 440 °C. (d) Detection limit of 30_$LaFeO_3/SnO_2$ NTs toward $C_2H_2$ gas down to 0.1 ppm. (e) Response time for 0, 10, 30 and 120_$LaFeO_3/SnO_2$ NTs. (f) Response *versus* $C_2H_2$ concentration for previously reported state-of-the-art $C_2H_2$ sensors.

Published on 17 October 2022. Downloaded by Korea Advanced Institute of Science & Technology / KAIST on 11/27/2022 3:29:05 PM.

To find the optimized acetylene sensing temperature, we compared the temperature-dependent sensing characteristics of the sensor based on 30_$LaFeO_3$/$SnO_2$ NTs as the representative sample in a concentration range of 1–5 ppm, since the 30_$LaFeO_3$/$SnO_2$ NTs contain appreciable amounts of both the p-type $LaFeO_3$ perovskite phase and the n-type $SnO_2$ phase and are therefore expected to have the largest number of p–n heterojunctions. As shown in Fig. 6a, among various operation temperatures of 400, 430, 440, 450, and 500 °C, the optimal working temperature was determined to be 440 °C considering the highest gas response ($R_{air}/R_{gas}$ = 32.1 to 5 ppm at 440 °C). Notably, the response decreases for higher temperature ($R_{air}/R_{gas}$ = 3.35 to 5 ppm at 500 °C), likely due to the accelerated desorption of surface-adsorbed oxygen species, which facilitates the complete oxidation of target gases into nonreactive gas species such as $CO_2$ or $H_2O$, thus leading to a low response.[45] Subsequently, we compared the dynamic responses of the sensors, measured at 440 °C (Fig. 6b). The 30_$LaFeO_3$/$SnO_2$ NTs sensor exhibited superior acetylene response ($R_{air}/R_{gas}$ = 32.1 at 5 ppm) over those based on 120_$LaFeO_3$/$SnO_2$ NTs ($R_{air}/R_{gas}$ = 18.3), 10_$LaFeO_3$/$SnO_2$ NTs ($R_{air}/R_{gas}$ = 4.8), and $LaFeO_3$ NTs ($R_{gas}/R_{air}$ = 1.03), demonstrating that the transformation of $LaFeO_3$ NTs to $LaFeO_3$/$SnO_2$ NTs by a controlled GRR process results in a significant improvement of their gas sensing performance, so long as the GRR is terminated at an appropriate reaction time. In addition, the XPS peak ratio of $O^-/O^{2-}$ in GRR treated 30_$LaFeO_3$/$SnO_2$ NTs is much higher than those of 0_$LaFeO_3$/$SnO_2$ NTs (Table S2†). This result directly indicates the tremendously increased amount of chemisorbed oxygen species on the surface of 30_$LaFeO_3$/$SnO_2$ NTs compared to that of 0_$LaFeO_3$/$SnO_2$ NTs due to a large amount of $SnO_2$ nanograins formed by GRR. An increase in the oxygen adsorption is advantageous to provide much increased chemical interaction sites, therefore increasing the response of chemiresistive sensors.[46] To investigate the selectivity of the 30_$LaFeO_3$/$SnO_2$ NTs sensor, the sensing properties of 30_$LaFeO_3$/$SnO_2$ NTs were investigated at 440 °C toward seven other potentially interfering gas species (2-propanol ($C_3H_8O$), acetone ($CH_3COCH_3$), methyl mercaptan ($CH_3SH$), ethanol ($C_2H_5OH$), dimethyl sulfide ($CH_3SCH_3$), sulfur dioxide ($SO_2$), ammonia ($NH_3$)), each at a concentration of 5 ppm (Fig. 6c). The 30_$LaFeO_3$/$SnO_2$ NTs, together with an overall enhancement in their sensor response, showed a distinct improvement in their selectivity toward acetylene against other interfering gases compared to that of pristine $LaFeO_3$ NTs. In particular, the perovskite $LaFeO_3$ is well-reported material for selective activation of the reaction between acetylene and chemisorbed oxygen species on $LaFeO_3$.[47,48] This would result in remarkably improved selectivity, owing to the heterogeneous configurations of p-type $LaFeO_3$ catalytic regions and n-type $SnO_2$ nanograins as main sensing layers. In addition, the 30_$LaFeO_3$/$SnO_2$ NTs could readily detect 0.1 ppm (=100 ppb) of acetylene with noticeable response value ($R_{air}/R_{gas}$ = 2.80) at 440 °C (Fig. 6d), with a limit of detection (LOD) that is presumably below this concentration. Considering that transformer oil is typically replaced once the dissolved acetylene concentration reaches a few hundred ppm, the $LaFeO_3$/$SnO_2$ based sensor with sufficient sensitivities in a wide range of acetylene concentrations seems to be practically viable for monitoring the service life of an electrical power transformer. As shown in Fig. 6e, the 30_$LaFeO_3$/$SnO_2$ NTs exhibited faster responding speeds (16 s at 5 ppm of acetylene) in comparison to the pristine $LaFeO_3$ NTs as well as other GRR-treated samples. This can be attributed to the contribution of both the mesoporous morphology, which provides many channels for gas diffusion, as well as the numerous active surface sites. Also, the 30_$LaFeO_3$/$SnO_2$ NTs exhibited a stable sensing behavior toward 5 ppm acetylene for 21 repeated cycles of exposure followed by recovery (Fig. S13†). Altogether, we found that the performance of 30_$LaFeO_3$/$SnO_2$ NTs based acetylene sensors are unparalleled to other SMO-based sensors reported in literature,[13,15,47,49–56] exemplifying the efficacy of GRR as a powerful strategy for engineering the composition and morphology toward optimizing the sensing characteristics of SMO-based materials (Fig. 6f).

## Conclusions

We have demonstrated the galvanic replacement reaction (GRR) based process to transform $LaFeO_3$ perovskite nanotubes (NTs) into heterogeneous oxide nanostructures with high porosity for highly sensitive and selective gas sensors toward acetylene. Due to the atomic scale replacement reaction between $SnO_2$ and $LaFeO_3$ at low reaction temperature (<90 °C), the numerous p–n heterogeneous junctions were naturally created within the tubular structure with high surface area (146.6 $m^2$ $g^{-1}$), thus exceptionally activating the selective chemical reaction to target acetylene molecules in $SnO_2$ nanograin (<10 nm) sensitized $LaFeO_3$ NTs. As a result, the GRR treated $LaFeO_3$/$SnO_2$ NTs exhibited significantly enhanced sensitivity to acetylene even at sub-1 ppm level of acetylene ($R_{air}/R_{gas}$ = 2.8 to 0.1 ppm) in a highly selective manner, even without using conventional noble metal catalysts. Based on our mechanistic study of the GRR process for perovskite oxides, we believe that our strategy has the potential for expansion toward perovskites and other complex oxides, each of which could be fine-tuned by varying GRR conditions to tailor them toward many industrially and scientifically relevant applications including electrocatalyst, energy storage materials, catalyst and sensors.

## Experimental section

### Preparation of precursor materials

Lanthanum nitrate hexahydrate $La(NO_3)_3 \cdot 6H_2O$, iron nitrate nonahydrate $Fe(NO_3)_3 \cdot 9H_2O$, tin chloride dihydrate ($SnCl_2 \cdot 2H_2O$), *N*,*N*-dimethylformamide, polyvinylpyrrolidone (PVP, $M_w$ = 1 300 000), xylene, oleic acid, oleylamine were purchased from Sigma-Aldrich (St. Louis. USA). Hydrochloric acid (HCl solution, 37%) were purchased from Samchun (South Korea). The precursor metal nitrates with purity 99.9% and all other chemicals were used as-received without any further purification.

### Synthesis of $LaFeO_3$ NTs

$LaFeO_3$ (LFO) nanotubes were synthesized by electrospinning. The precursor solution was prepared by the following procedure. The stoichiometric amounts of 1.0825 g of $La(NO_3)_3 \cdot 6H_2O$

 This journal is © The Royal Society of Chemistry 2022

Published on 17 October 2022. Downloaded by Korea Advanced Institute of Science & Technology / KAIST on 11/27/2022 3:29:05 PM.

and 1.0100 g of $Fe(NO_3)_3 \cdot 9H_2O$ precursor salts were dissolved in 9.44 g of DMF solvents. Then, 1.422 g of polyvinylpyrrolidone (PVP) was gently added to the composite metal nitrate solutions and stirred 12 hours. The precursor solution was then transferred into 20 mL plastic syringes and electrospun with a pump at a feeding rate of 10 μL $min^{-1}$, a high voltage of 15 kV, and a distance between the tip of the syringe nozzle and the drum collector of 15 cm. After the electrospinning, as-spun composite nanofibers (La and Fe precursors, PVP) were calcined at 450 °C and 700 °C for 2 hours, respectively at a heating rate of 5 °C $min^{-1}$ in ambient atmosphere to obtain the crystalline perovskite phase $LaFeO_3$ NTs.

### Galvanic replacement reaction of $LaFeO_3$ NTs with $Sn^{2+}$ ions

In order to synthesize the $LaFeO_3/SnO_2$ NTs, the 0.08 g of as prepared $LaFeO_3$ NTs were dispersed in 10 mL of xylene solvents with 0.14 g of oleic acid and 2.00 g of oleylamine. This composite solution was placed in oil bath and heated to 90 °C on a hot plate. In the meanwhile, $SnCl_2 \cdot 2H_2O$ (4 mmol in 2 mL of deionized water) solution were mixed with 0.5 mL of HCl (37%) to complete dissolution of stannous salt in water. This Sn precursor solutions were gently poured into the composite solution of $LaFeO_3$ NTs. Note that the 30_$LaFeO_3/SnO_2$ NTs can be achieved through the aforementioned GRR process after 30 min. The resulting galvanically reacted $LaFeO_3$ NTs powder was collected by centrifugation and washed several times with ethanol. Finally, the product was then dried in oven at 60 °C for 12 h. All the synthetic procedures of $LaFeO_3/SnO_2$ NTs were the same except the different duration time in GRR process.

### Material characterization

To confirm the change in microstructures and morphologies of the electrospun and galvanic reaction treated $LaFeO_3$ NTs, field emission scanning electron microscope (SEM, SU8230, Hitachi), 300 keV field emission transmission electron microscope (Fe-TEM, F30 super-twin, Tecnai) and field emission scanning transmission electron microscope (FE-STEM, HD-2300A, Hitachi) were used. High resolution powder X-ray diffractometer (RIGAKU, SmartLab) with Cu Kα radiation ($\lambda = 1.5418$ Å) was used to confirm the crystal structure of each samples. The chemical bonding states of each samples were investigated by X-ray photoelectron spectroscopy (XPS, Axis-Supra, Kratos) with Al K radiation. The Brunauer–Emmett–Teller (BET) surface area and pore size distribution of the samples confirmed by using $N_2$ adsorption/desorption isotherms (Tristar 3020, Micromeritics 0 at 77 K). Ultraviolet photoelectron spectroscopy (UPS) measurements were conducted with an AXIS-Supra using a He I discharge lamp that has 21.2 eV of photon energy. A UV-vis spectrometer (Shimadzu UV-1800) was used to obtain the UV-vis absorbance spectrum.

### Evaluation of gas sensing performance

To measure the gas sensing characteristics, we prepared gas sensors on $Al_2O_3$ substrates patterned with two parallel Au electrodes on the front side and Pt heater lines on the back side. 3 mg of the prepared sensing materials were dispersed in 150 μL of ethanol. Next, the dispersed solutions for each sample were drop-coated on the front side of the substrate where a pair of interdigitated Au electrodes (25 μm width and 150 μm electrode gap) were printed on one side of the $Al_2O_3$ substrate and Pt heater lines were attached to the other side. All the sensors were stabilized under ambient conditions for 3 h before gas in. To investigate the response to the target gas, the sensors were exposed to 8 different gas species (acetylene, 2-propanol, acetone, methyl mercaptan, ethanol, dimethyl sulfide, sulfur dioxide, ammonia). The target gases were purchased from a specialized vendor in the form of pressurized gas bombes calibrated to the specified concentration. The gas bombes, including those of balance gases such as air, were attached to mass flow controllers (MFC) for computer-controlled flow and mixing. The relative proportions of the target gas to the balance gas were modified for each experiment while keeping the total gas flow fixed at 1000 sccm. The humidity of the balance gas was controlled by diverting a portion of the gas flow into a water bubbler held at 37 °C, and then mixing this wet gas back with the pristine balance gas using the MFC. We measured the resistance changes of each samples by using a data acquisition system (34972A, Agilent), and the obtained data were translated into gas response, *i.e.*, resistance ratio of $R_{air}/R_{gas}$ or $R_{gas}/R_{air}$, where $R_{air}$ is the baseline resistance in ambient air and $R_{gas}$ is the resistance shown in period of gas injection. The response time is defined as the time for the increase of the resistance from $R_{air}$ to 90% of $\Delta R_{max}$. The on/off interval of exposure to gases was 10 min. The operation temperature was adjusted by applying a DC voltage to the Pt microheater using a DC power supply (E3644A, Agilent). Temperature of the heating system can be altered by applying different voltages (*e.g.* 6.34 V = 440 °C).

## Author contributions

J. W. B conceived the concept and designed the whole project including all experiments. J. W. B and Y. W. K conducted the overall experiment, characterization, and analysis of results. J. A. assisted literature survey and helped to draft the manuscript. D. K., H. S., J. K., S. P., C. P., and E. C. provided purely technical support and helped edit the manuscript. All authors discussed the results and contributed to the manuscript. J. S. J. and I. D. K. were responsible for managing all aspects of this project.

## Conflicts of interest

There are no conflicts to declare.

## Acknowledgements

This work was supported by the National Research Foundation of Korea (NRF) grant funded by the Ministry of Science and ICT of the Government of the Republic of Korea (Grant No. 2020R1A2C301312711). This work was also supported by Nano Convergence Foundation funded by the Ministry of Science and ICT (MSIT, Korea) & the Ministry of Trade, Industry and Energy (MOTIE, Korea) (No. 20000230).

Published on 17 October 2022. Downloaded by Korea Advanced Institute of Science & Technology / KAIST on 11/27/2022 3:29:05 PM.

## Notes and references


1 D. A. Sarigiannis, M. Kermenidou, S. Nikolaki, D. Zikopoulos and S. P. Karakitsios, *Aerosol Air Qual. Res.*, 2015, **15**, 2496–2507.
2 Y. O. Khaniabadi, S. M. Daryanoosh, A. Amrane, R. Polosa, P. K. Hopke, G. Goudarzi, M. J. Mohammadi, P. Sicard and H. Armin, *Atmos. Pollut. Res.*, 2017, **8**, 606–613.
3 S.-J. Kim, S.-J. Choi, J.-S. Jang, H.-J. Cho and I.-D. Kim, *Acc. Chem. Res.*, 2017, **50**, 1587–1596.
4 B. Kwon, H. Bae, H. Lee, S. Kim, J. Hwang, H. Lim, J. H. Lee, K. Cho, J. Ye and S. Lee, *ACS Nano*, 2022, **16**, 2176–2187.
5 R. Malik, V. K. Tomer, Y. K. Mishra and L. Lin, *Appl. Phys. Rev.*, 2020, **7**, 021301.
6 A. Dey, *Mater. Sci. Eng., B*, 2018, **229**, 206–217.
7 G. Mamba, P. Mafa, V. Muthuraj, A. Mashayekh-Salehi, S. Royer, T. Nkambule and S. Rtimi, *Mater. Today Nano*, 2022, 100184.
8 X. Xu and X. Wang, *Small Struct.*, 2020, **1**, 2000009.
9 G. Zhang, X.-Z. Song, X.-F. Wang, N. Liu, X. Li, Z. Wei, G. Qian, Z. Wang, S. Yu and Z. Tan, *J. Alloys Compd.*, 2022, **902**, 163803.
10 K. Pirkanniemi and M. Sillanpää, *Chemosphere*, 2002, **48**, 1047–1060.
11 Z. Zhang, C. Shao, X. Li, C. Wang, M. Zhang and Y. Liu, *ACS Appl. Mater. Interfaces*, 2010, **2**, 2915–2923.
12 H.-J. Kim and J.-H. Lee, *Sens. Actuators, B*, 2014, **192**, 607–627.
13 A. A. Alharbi, A. Sackmann, U. Weimar and N. Bârsan, *Sens. Actuators, B*, 2022, **353**, 131079.
14 L. Sun, H. Qin, K. Wang, M. Zhao and J. Hu, *Mater. Chem. Phys.*, 2011, **125**, 305–308.
15 A. Sukee, A. Alharbi, A. Staerz, A. Wisitsoraat, C. Liewhiran, U. Weimar and N. Barsan, *Sens. Actuators, B*, 2020, **312**, 127990.
16 N. Zhang, S. Ruan, Y. Yin, F. Li, S. Wen and Y. Chen, *ACS Appl. Nano Mater.*, 2018, **1**, 4671–4681.
17 T. T. N. Phan, T. T. M. Dinh, M. D. Nguyen, D. Li, C. N. Phan, T. K. Pham, C. T. Nguyen and T. H. Pham, *Sens. Actuators, B*, 2022, **354**, 131195.
18 W. Qin, R. Zhang, Z. Yuan, C. Xing and F. Meng, *IEEE Trans. Instrum. Meas.*, 2022, **71**, 1–9.
19 M. H. Oh, T. Yu, S.-H. Yu, B. Lim, K.-T. Ko, M.-G. Willinger, D.-H. Seo, B. H. Kim, M. G. Cho, J.-H. Park, K. Kang, Y.-E. Sung, N. Pinna and T. Hyeon, *Science*, 2013, **340**, 964–968.
20 H.-M. Jeong, J.-H. Kim, S.-Y. Jeong, C.-H. Kwak and J.-H. Lee, *ACS Appl. Mater. Interfaces*, 2016, **8**, 7877–7883.
21 J.-S. Jang, W.-T. Koo, S.-J. Choi and I.-D. Kim, *J. Am. Chem. Soc.*, 2017, **139**, 11868–11876.
22 J. S. Jang, S. E. Lee, S. J. Choi, W. T. Koo, D. H. Kim, H. Shin, H. J. Park and I. D. Kim, *Adv. Funct. Mater.*, 2019, **29**, 1903012.
23 Y. Zhang, Z. Duan, H. Zou and M. Ma, *Mater. Lett.*, 2018, **215**, 58–61.
24 Y. Ye, H. Yang, H. Zhang and J. Jiang, *Environ. Technol.*, 2020, **41**, 1486–1503.
25 S. Zhao, Y. Wang, L. Wang and Y. Jin, *Inorg. Chem. Front.*, 2017, **4**, 994–1002.
26 M. A. Hossain, J. R. Jennings, Z. Y. Koh and Q. Wang, *ACS Nano*, 2011, **5**, 3172–3181.
27 Z. Dai, C.-S. Lee, B.-Y. Kim, C.-H. Kwak, J.-W. Yoon, H.-M. Jeong and J.-H. Lee, *ACS Appl. Mater. Interfaces*, 2014, **6**, 16217–16226.
28 K. Cao, E. Cao, Y. Zhang, W. Hao, L. Sun and H. Peng, *Sens. Actuators, B*, 2016, **230**, 592–599.
29 J. Ning, J. Wang, X. Li, T. Qiu, B. Luo, L. Hao, M. Liang, B. Wang and L. Zhi, *J. Mater. Chem. A*, 2014, **2**, 10969–10973.
30 S. Wang, W. Yu, C. Cheng, T. Zhang, M. Ge, Y. Sun and N. Dai, *Mater. Res. Bull.*, 2017, **89**, 267–272.
31 J. H. Pan, Z. Lei, W. I. Lee, Z. Xiong, Q. Wang and X. Zhao, *Catal. Sci. Technol.*, 2012, **2**, 147–155.
32 V. Bonu, A. Das, A. K. Prasad, N. G. Krishna, S. Dhara and A. Tyagi, *Appl. Phys. Lett.*, 2014, **105**, 243102.
33 Y. Tong, Y. Zhang, B. Jiang, J. He, X. Zheng and Q. Liang, *IEEE Sens. J.*, 2017, **17**, 2404–2410.
34 H. Aono, M. Sato, E. Traversa, M. Sakamoto and Y. Sadaoka, *J. Am. Ceram. Soc.*, 2001, **84**, 341–347.
35 H.-J. Cho, S.-J. Choi, N.-H. Kim and I.-D. Kim, *Sens. Actuators, B*, 2020, **304**, 127350.
36 A. Rothschild and Y. Komem, *J. Appl. Phys.*, 2004, **95**, 6374–6380.
37 C. Xu, J. Tamaki, N. Miura and N. Yamazoe, *Sens. Actuators, B*, 1991, **3**, 147–155.
38 M. Duval, *IEEE Elect. Insul. Mag.*, 1989, **5**, 22–27.
39 M. Metsälä, F. M. Schmidt, M. Skyttä, O. Vaittinen and L. Halonen, *J. Breath Res.*, 2010, **4**, 046003.
40 D. Marchenko, A. Neerincx, J. Mandon, J. Zhang, M. Boerkamp, J. Mink, S. Cristescu, S. te Lintel Hekkert and F. Harren, *Appl. Phys. B*, 2015, **118**, 275–280.
41 N. R. Williams and R. M. Whittington, *J. Toxicol., Clin. Toxicol.*, 2001, **39**, 69–71.
42 J. S. Jang, S. Yu, S. J. Choi, S. J. Kim, W. T. Koo and I. D. Kim, *Small*, 2016, **12**, 5989–5997.
43 W. Zhang, C. Xie, G. Zhang, J. Zhang, S. Zhang and D. Zeng, *Mater. Chem. Phys.*, 2017, **186**, 228–236.
44 M. Mashock, K. Yu, S. Cui, S. Mao, G. Lu and J. Chen, *ACS Appl. Mater. Interfaces*, 2012, **4**, 4192–4199.
45 I.-D. Kim, A. Rothschild, B. H. Lee, D. Y. Kim, S. M. Jo and H. L. Tuller, *Nano Lett.*, 2006, **6**, 2009–2013.
46 L. Gao, F. Ren, Z. Cheng, Y. Zhang, Q. Xiang and J. Xu, *CrystEngComm*, 2015, **17**, 3268–3276.
47 A. Alharbi, A. Sackmann, U. Weimar and N. Bârsan, *Sens. Actuators, B*, 2020, **303**, 127204.
48 A. A. Alharbi, A. Sackmann, U. Weimar and N. Bârsan, *J. Phys. Chem. C*, 2020, **124**, 7317–7326.
49 N. Zhang, Y. Fan, Y. Lu, C. Li, J. Zhou, X. Li, S. Adimi and S. Ruan, *Sens. Actuators, B*, 2020, **307**, 127629.
50 A. I. Uddin and G.-S. Chung, *Oxide-based Materials and Devices VII*, 2016.
51 Y. Lin, C. Li, W. Wei, Y. Li, S. Wen, D. Sun, Y. Chen and S. Ruan, *RSC Adv.*, 2015, **5**, 61521–61527.


 This journal is © The Royal Society of Chemistry 2022

Published on 17 October 2022. Downloaded by Korea Advanced Institute of Science & Technology / KAIST on 11/27/2022 3:29:05 PM.

52 X. Gao, Q. Zhou, Z. Lu, L. Xu, Q. Zhang and W. Zeng, *Front. Mater.*, 2019, **6**, 163.
53 A. I. Uddin, K.-W. Lee and G.-S. Chung, *Sens. Actuators, B*, 2015, **216**, 33–40.
54 X. Wang, M. Zhao, F. Liu, J. Jia, X. Li and L. Cao, *Ceram. Int.*, 2013, **39**, 2883–2887.
55 Q. Qi, T. Zhang, X. Zheng, H. Fan, L. Liu, R. Wang and Y. Zeng, *Sens. Actuators, B*, 2008, **134**, 36–42.
56 N. Tamaekong, C. Liewhiran, A. Wisitsoraat and S. Phanichphant, *Sens. Actuators, B*, 2011, **152**, 155–161.